Simultaneous decoherence and mode filtering in quantum channels: theory and experiment

Gabriele Riccardi* and Cristian Antonelli†
Department of Physical and Chemical Sciences
University of L'Aquila, 67100 L'Aquila, Italy

Daniel E. Jones‡ and Michael Brodsky§
U.S. Army Research Laboratory
2800 Powder Mill Road, Adelphi, MD 20783-1197
(Dated: February 8, 2021)

Quantum networks require robust quantum channels for fast and reliable entanglement distribution over long distances. As quantum communication technology matures, it moves towards utilizing actual fibers and free space optical channels, hence there is a growing need for physical models describing decoherence in fibers and in a turbulent atmosphere. The primary challenge is to concisely account for numerous elements distributed along a lengthy optical path. We approach this by starting with an analytical model of a channel with just two lumped elements, one representing decoherence and the other representing mode filtering. Interestingly, we find that while the order and relative orientation of the two elements produce a wealth of different bi-photon states, the amount of entanglement in all those states is exactly the same. Then, we conduct experiments that implement this channel and verify our analytical findings. Finally, we expand our analysis to the most general channel, resulting from a statistically significant number of arbitrarily oriented elements. We show that over an ample range of parameters, our two-element analytical model is quite accurate in describing the general channel, which makes it an effective tool for gaining insights into channel decoherence.

I. INTRODUCTION

The booming field of quantum information science calls for new approaches to storing, handling, computing, and communicating information. What began as a purely theoretical quest a few decades ago has recently expanded into the realm of lab and field demonstrations of a number of applications. For one, both classical and quantum secret sharing were realized in an untrusted node scenario with the use of 5-qubit graph states [1], in multi-dimensional spaces by using vectorially structured photons that enabled encoding in both polarization and their optical orbital momentum [2], and between the cores of a multi-core fiber [3]. A proof-of-principle concept of measurement-device-independent quantum digital signatures was implemented in a three node network [4]. Wang et al. experimentally probed the efficacy of entanglement-assisted quantum metrology against amplitude-damping, depolarizing, and general Pauli channels [5]. Finally, recent studies produced the theoretical groundwork for entanglement-assisted sensing in the radio- and microwave spectral ranges [6] and a delineation of quantum advantages of high-dimensional quantum illumination [7]. The common motif of the above-mentioned results is distributed entanglement. That is, each protocol relies on an entangled state being pre-shared between distant parties by transmission over quantum channels.

Quantum channels themselves received ample attention in the recent literature from both theoretical and experimental flanks. The advances from the two sides are drastically different though and are somewhat disjoint. On one hand, information theory targets channel capacity bounds for conventional Pauli-channel models. Advances in approximating physically unavailable channels by combinations of Pauli channels [8] are complimented by simulations of Pauli-damping channels [9]; a lower bound to the Holevo capacity was calculated for higher-dimensional Pauli, dephasing, and depolarizing channels [10]; and entanglement cost expressions were obtained for a number of cases such as dephasing, erasure, three-dimensional Werner-Holevo channels, and bosonic Gaussian channels [11]. On the other hand, we see experiments aiming at building exotic channels for quantum-information transfer. Bidirectional quantum links were constructed from paired polarization-maintaining fibers [12]; chiral waveguides were predicted to be able to reliably transfer Bell states, high-dimensional W-states, and Dicke states all in the presence of noise [13]; special air-core fibers were exploited to transfer quantum information encoded in a photon's orbital angular momentum (OAM) [14]; and some combination of OAM and polarization encoding was proven effective over short distances in 850-nm single-mode fibers [15].

In addition to these remarkable achievements, successful deployment of quantum systems over either con-

* gabriele.riccardi@graduate.univaq.it
† cristian.antonelli@univaq.it; Also at National Inter-University Consortium for Telecommunications - CNIT, Italy
‡ daniel.e.jones161.civ@mail.mil
§ michael.brodsky4.civ@mail.mil; Also at U.S. Military Academy, West Point, NY 10996, USA

ventional telecom fibers or free-space ground-to-satellite channels was demonstrated by several groups. For time-bin photon encoding, a three-user star-topology metropolitan network was constructed for measurement-device-independent (MDI) quantum key distribution (QKD) over 30km of fiber in Hefei [16]. In parallel, Calgary's fiber network was used for quantum teleportation by performing a Bell state measurement at the central node [17]. A truly record-breaking 421km QKD link length was achieved by improving rate and detector efficiencies [18], only to be soon surpassed by a 502 km transmission using phase-matched QKD [19]. Finally, polarization encoding enabled two more major recent developments. First, an uplink ground-to-satellite teleportation was demonstrated despite challenges of turbulence-induced beam broadening and wandering [20]. Second, one photon of an EPR pair was sent over a 96km [21] and 192 km [22] submarine fiber while preserving its entanglement with the other photon.

Naturally, there is a growing body of work aimed at developing the understanding of real-life quantum channels. This includes channel characterization techniques leveraging classical light [23, 24] and methods for assessing non-entanglement-breaking channel properties. Examples are the recently proposed application of signaling games to the certification of noise-added channels [25], as well as MDI verification for channels impaired by depolarizing and dephasing noise [26]. Further studies aim at uncovering pertinent decoherence mechanisms for real-life channels, such as dynamical dephasing due to refractive-index fluctuations [27, 28]. Entanglement could also be affected by the geometry of the optical beam. For instance, atmospheric turbulence may cause beam wandering and broadening, as well as beam-shape deformation [29–32]. Equivalent mechanisms manifest themselves in fiber-optic networks in the form of Polarization Mode Dispersion (PMD) and Polarization Dependent Loss (PDL), which are individually known to affect entanglement distribution in quantum communication experiments [33–35] and [36–38], respectively. The interplay of those two phenomena, that are usually present simultaneously in fiber quantum channels, is tremendously complex and is not fully understood. Therefore, there exists a need for intuitive models that provide experimentalists with handy tools to characterize and emulate fiber channels while reliably capturing the essence of this interplay.

In this paper, we provide a comprehensive model describing the joint effect of decoherence and mode filtering on a travelling EPR pair. For polarization-entangled photons transmitted in quantum fiber channels, both effects are generally distributed along the photon path in the form of PMD and PDL. Here, however, we start by considering the simple case of just two lumped elements in one channel, one causing decoherence and another causing partial mode filtering. Since environmental changes affect the relative orientation of the corresponding eigenstates on the Bloch sphere, we explore the effect of the elements' orientation. We also examine the impact of the order in which they affect the travelling photon to account for opposite propagation direction. We provide experimental verification of our model in the most illustrative cases and establish peculiar symmetries of the propagated bi-photon states. We then expand our analytical results to model a general fiber-optic channel, where the effect of a multitude of small decoherence and mode-filtering elements accumulates along the route in a random fashion. We numerically investigate the effect of such a general channel and determine boundaries within which it can be reasonably approximated by the much simpler and physically intuitive channel consisting of just two lumped elements.

The paper is organized as follows. In Section II, we introduce our model for the joint effect of lumped decoherence and mode-filtering elements in the optical path of one of two polarization-entangled photons on the quantum properties of the received two-photon state. In Section III, we present experimental results pertaining to the main implications of the model and explore the concept of nonlocal compensation of mode-filtering. In Section IV, we discuss how a quantum channel formed by a filtering element and a decohering element is representative of a general fiber-optic channel operated in the linear propagation regime. Finally, we draw our conclusions in Section V.

II. EFFECT OF CASCADED DECOHERENCE AND FILTERING ON POLARIZATION-ENTANGLED PHOTONS

While photons can be entangled in various physical dimensions, in this work we focus on polarization as the most ubiquitous degree of freedom. We consider a pair of polarization-entangled photons, where one photon, which we refer to as photon A, propagates through a fiber channel, and the second photon stays in the proximity of the source and experiences no propagation effects. Here we study the most general channel resulting from the concatenation of two elements - a decoherence element and a mode-filtering one. Our main goal is to characterize the dependence of the propagated state's quantum properties on the details of the channel implementation, that is the order in which decoherence and modal filtering act on the transmitted photon and their relative orientation. The order of the two elements is representative of how the two effects occur along the photon propagation path, as well as of the bidirectionality of a channel. The relative orientation of the elements captures the changes of the eigenstates of each of the two polarization effects. These are ever-present in fiber routes due to changing ambient conditions [39, 40].

We start by expressing the state of the polarization-entangled photon pair in the frequency domain, which facilitates a comparison with the experimental setup used in this work. Consistent with our setup, we assume a

pulsed-pump source based on a $\chi^{(3)}$ medium, for which the generated two-photon state is

$$|\psi_{\rm in}\rangle = |\tilde{f}(\omega_A,\omega_B)\rangle \otimes \frac{|\boldsymbol{h}_A\boldsymbol{h}_B\rangle + |\boldsymbol{h}'_A\boldsymbol{h}'_B\rangle}{\sqrt{2}}, \quad (1)$$

where $(\boldsymbol{h}_A,\boldsymbol{h}'_A)$ and $(\boldsymbol{h}_B,\boldsymbol{h}'_B)$ denote two bases of orthogonal polarization states for photons A and B, respectively, and where

$$|\tilde{f}(\omega_A,\omega_B)\rangle = \int\int d\omega_A d\omega_B \tilde{f}(\omega_A,\omega_B)\,|\omega_A,\omega_B\rangle\,, \quad (2)$$

with

$$\tilde{f}(\omega_A,\omega_B) = H_A(\omega_A)H_B(\omega_B) \times \int d\omega' \tilde{E}_p(\omega')\tilde{E}_p(\omega_A+\omega_B-\omega'). \quad (3)$$

Here, $\tilde{E}_p(\omega)$ denotes the Fourier transform of the pump waveform $E_p(t)$, and $H_A(\omega_A)$ and $H_B(\omega_B)$ denote the transfer functions of the filters applied to the two photons prior to transmission. The time-domain equivalent of Eq. (1) is

$$|\psi_{\rm in}\rangle = |f(t_A,t_B)\rangle \otimes \frac{|\boldsymbol{h}_A\boldsymbol{h}_B\rangle + |\boldsymbol{h}'_A\boldsymbol{h}'_B\rangle}{\sqrt{2}}, \quad (4)$$

where

$$|f(t_A,t_B)\rangle = \int\int dt_A dt_B f(t_A,t_B)|t_A,t_B\rangle, \quad (5)$$

with $f(t_A,t_B)$ being the inverse Fourier transform of $\tilde{f}(\omega_A,\omega_B)$.

We now denote by $\boldsymbol{\gamma}$ the Stokes vector associated with the mode-filtering element, whose effect is described by the operator $\mathbf{T}_0 = \exp(\boldsymbol{\gamma}\cdot\boldsymbol{\sigma}/2)$, where $\boldsymbol{\sigma}$ is a vector whose elements are the three Pauli matrices, so that $\boldsymbol{\gamma}\cdot\boldsymbol{\sigma} = \gamma_1\sigma_1+\gamma_2\sigma_2+\gamma_3\sigma_3$. With no loss of generality, we assume that the z axis in Stokes space corresponds to the polarization state $\boldsymbol{h}_A$ and that $\boldsymbol{\gamma}$ is aligned with it, in which case the mode-filtering operator simplifies to the following diagonal form:

$$\mathbf{T}_0 = \begin{pmatrix} e^{\gamma/2} & 0 \\ 0 & e^{-\gamma/2} \end{pmatrix} \quad (6)$$

in the $(\boldsymbol{h}_A,\boldsymbol{h}'_A)$ basis, where $\gamma = |\boldsymbol{\gamma}|$. On the other hand, the effect of the birefringent decohering element characterized by the Stokes vector $\boldsymbol{\tau}$ is described by the operator $\mathbf{U}(\omega) = \exp(-i\omega\boldsymbol{\tau}\cdot\boldsymbol{\sigma}/2)$ [41], where $\boldsymbol{p}_A$ and $\boldsymbol{p}'_A$ denote its orthogonal eigenstates, and ω is the offset from the carrier frequency. The polarization basis $(\boldsymbol{p}_A,\boldsymbol{p}'_A)$ can be used to re-express the input state as

$$|\psi_{\rm in}\rangle = |f(t_A,t_B)\rangle \otimes \frac{|\boldsymbol{p}_A\boldsymbol{p}_B\rangle + |\boldsymbol{p}'_A\boldsymbol{p}'_B\rangle}{\sqrt{2}}, \quad (7)$$

where by $(\boldsymbol{p}_B,\boldsymbol{p}'_B)$ we denote an auxiliary orthogonal basis for the polarization of photon B given by $|\boldsymbol{p}_B\rangle = \langle\boldsymbol{p}_A|\boldsymbol{h}_A\rangle\,|\boldsymbol{h}_B\rangle + \langle\boldsymbol{p}_A|\boldsymbol{h}'_A\rangle\,|\boldsymbol{h}'_B\rangle$ and $|\boldsymbol{p}'_B\rangle = \langle\boldsymbol{p}'_A|\boldsymbol{h}_A\rangle\,|\boldsymbol{h}_B\rangle + \langle\boldsymbol{p}'_A|\boldsymbol{h}'_A\rangle\,|\boldsymbol{h}'_B\rangle$ [35]. In the basis $(\boldsymbol{p}_A,\boldsymbol{p}'_A)$, the effect of decoherence simplifies to a relative delay $\tau = |\boldsymbol{\tau}|$ between the polarization states $\boldsymbol{p}_A$ and $\boldsymbol{p}'_A$.

The first channel configuration that we consider is the one in which the modal filtering element precedes the decohering element (in what follows we refer to this configuration as *filtering-first*). In this case, the output state is obtained by first applying the filtering operator to Eq. (1) and then expressing the resulting state in the $(\boldsymbol{p}_A,\boldsymbol{p}'_A)$ basis prior to applying the decohering operator. This results in the output state

$$\begin{aligned}|\psi_{\rm out}\rangle = & \frac{\eta}{\sqrt{2}}|f(t_A-\tau/2,t_B)\rangle \otimes \\ & (e^{\frac{\gamma}{2}}\langle\boldsymbol{p}_A|\boldsymbol{h}_A\rangle|\boldsymbol{p}_A\boldsymbol{h}_B\rangle + e^{-\frac{\gamma}{2}}\langle\boldsymbol{p}_A|\boldsymbol{h}'_A\rangle|\boldsymbol{p}_A\boldsymbol{h}'_B\rangle) \\ & + \frac{\eta}{\sqrt{2}}|f(t_A+\tau/2,t_B)\rangle \otimes \\ & (e^{\frac{\gamma}{2}}\langle\boldsymbol{p}'_A|\boldsymbol{h}_A\rangle|\boldsymbol{p}'_A\boldsymbol{h}_B\rangle + e^{-\frac{\gamma}{2}}\langle\boldsymbol{p}'_A|\boldsymbol{h}'_A\rangle|\boldsymbol{p}'_A\boldsymbol{h}'_B\rangle), \end{aligned} \quad (8)$$

where the normalization coefficient η accounts for the fact that the state is post-selected by coincidence measurement.

In the second channel configuration that we consider, decoherence precedes mode-filtering (in what follows we refer to this configuration as *decoherence-first*). In this case, the output state is obtained by first applying the decohering operator to Eq. (7) and then expressing the resulting state in the $(\boldsymbol{h}_A,\boldsymbol{h}'_A)$ basis prior to applying the filtering operator. This results in the state

$$\begin{aligned}|\psi_{\rm out}\rangle = & \frac{\eta}{\sqrt{2}}|f(t_A-\tau/2,t_B)\rangle \otimes \\ & (e^{\frac{\gamma}{2}}\langle\boldsymbol{h}_A|\boldsymbol{p}_A\rangle|\boldsymbol{h}_A\boldsymbol{p}_B\rangle + e^{-\frac{\gamma}{2}}\langle\boldsymbol{h}'_A|\boldsymbol{p}_A\rangle|\boldsymbol{h}'_A\boldsymbol{p}_B\rangle) \\ & + \frac{\eta}{\sqrt{2}}|f(t_A+\tau/2,t_B)\rangle \otimes \\ & (e^{\frac{\gamma}{2}}\langle\boldsymbol{h}_A|\boldsymbol{p}'_A\rangle|\boldsymbol{h}_A\boldsymbol{p}'_B\rangle + e^{-\frac{\gamma}{2}}\langle\boldsymbol{h}'_A|\boldsymbol{p}'_A\rangle|\boldsymbol{h}'_A\boldsymbol{p}'_B\rangle). \end{aligned} \quad (9)$$

The density matrix ρ characterizing the polarization properties of the received state is then obtained in both cases by tracing the full density matrix $|\psi_{\rm out}\rangle\langle\psi_{\rm out}|$ over the time modes. To this end, it is convenient to introduce the function $R(\tau)$, defined as

$$R(\tau) = \int\int d\omega_A d\omega_B |\tilde{f}(\omega_A,\omega_B)|^2 e^{i\omega_A\tau}. \quad (10)$$

When expressed in the time domain, this function describes the overlap integral between the original waveform and its delayed replica. Note that once the time modes have been traced out, all the system parameters that affect the time/frequency-dependent part of the received two-photon state (primarily the pump and filter characteristics and the magnitude of the decohering element) only enter the resulting density matrix through this function. Specifically, assuming that $\tilde{f}$ is normalized so that $R(0) = 1$, the elements of the resulting density

matrix for the *filtering-first* case are

$$\begin{aligned}
&\rho_{11} = e^{\gamma}|\langle \boldsymbol{p}_A|\boldsymbol{h}_A\rangle|^2\eta^2/2,\ \rho_{22} = e^{-\gamma}|\langle \boldsymbol{p}_A|\boldsymbol{h}'_A\rangle|^2\eta^2/2\\
&\rho_{33} = e^{\gamma}|\langle \boldsymbol{p}'_A|\boldsymbol{h}_A\rangle|^2\eta^2/2,\ \rho_{44} = e^{-\gamma}|\langle \boldsymbol{p}'_A|\boldsymbol{h}'_A\rangle|^2\eta^2/2\\
&\rho_{12} = \langle \boldsymbol{p}_A|\boldsymbol{h}_A\rangle\langle \boldsymbol{p}_A|\boldsymbol{h}'_A\rangle^*\eta^2/2\\
&\rho_{13} = e^{\gamma}R^*(\tau)\langle \boldsymbol{p}_A|\boldsymbol{h}_A\rangle\langle \boldsymbol{p}'_A|\boldsymbol{h}_A\rangle^*\eta^2/2\\
&\rho_{14} = R^*(\tau)\langle \boldsymbol{p}_A|\boldsymbol{h}_A\rangle\langle \boldsymbol{p}'_A|\boldsymbol{h}'_A\rangle^*\eta^2/2\\
&\rho_{23} = R^*(\tau)\langle \boldsymbol{p}_A|\boldsymbol{h}'_A\rangle\langle \boldsymbol{p}'_A|\boldsymbol{h}_A\rangle^*\eta^2/2\\
&\rho_{24} = e^{-\gamma}R^*(\tau)\langle \boldsymbol{p}_A|\boldsymbol{h}'_A\rangle\langle \boldsymbol{p}'_A|\boldsymbol{h}'_A\rangle^*\eta^2/2\\
&\rho_{34} = \langle \boldsymbol{p}'_A|\boldsymbol{h}_A\rangle\langle \boldsymbol{p}'_A|\boldsymbol{h}'_A\rangle^*\eta^2/2.
\end{aligned} \tag{11}$$

Similarly, for the *decoherence-first* case, they are

$$\begin{aligned}
&\rho_{11} = e^{\gamma}|\langle \boldsymbol{h}_A|\boldsymbol{p}_A\rangle|^2\eta^2/2,\ \rho_{22} = e^{\gamma}|\langle \boldsymbol{h}_A|\boldsymbol{p}'_A\rangle|^2\eta^2/2\\
&\rho_{33} = e^{-\gamma}|\langle \boldsymbol{h}'_A|\boldsymbol{p}_A\rangle|^2\eta^2/2,\ \rho_{44} = e^{-\gamma}|\langle \boldsymbol{h}'_A|\boldsymbol{p}'_A\rangle|^2\eta^2/2\\
&\rho_{12} = e^{\gamma}R^*(\tau)\langle \boldsymbol{h}_A|\boldsymbol{p}_A\rangle\langle \boldsymbol{h}_A|\boldsymbol{p}'_A\rangle^*\eta^2/2\\
&\rho_{13} = \langle \boldsymbol{h}_A|\boldsymbol{p}_A\rangle\langle \boldsymbol{h}'_A|\boldsymbol{p}_A\rangle^*\eta^2/2\\
&\rho_{14} = R^*(\tau)\langle \boldsymbol{h}_A|\boldsymbol{p}_A\rangle\langle \boldsymbol{h}'_A|\boldsymbol{p}'_A\rangle^*\eta^2/2\\
&\rho_{23} = R(\tau)\langle \boldsymbol{h}_A|\boldsymbol{p}'_A\rangle\langle \boldsymbol{h}'_A|\boldsymbol{p}_A\rangle^*\eta^2/2\\
&\rho_{24} = \langle \boldsymbol{h}_A|\boldsymbol{p}'_A\rangle\langle \boldsymbol{h}'_A|\boldsymbol{p}'_A\rangle^*\eta^2/2\\
&\rho_{34} = e^{-\gamma}R^*(\tau)\langle \boldsymbol{h}'_A|\boldsymbol{p}_A\rangle\langle \boldsymbol{h}'_A|\boldsymbol{p}'_A\rangle^*\eta^2/2.
\end{aligned} \tag{12}$$

Note that in the first case, the density matrix is represented in the basis $|\boldsymbol{p}_A\boldsymbol{h}_B\rangle$, $|\boldsymbol{p}_A\boldsymbol{h}'_B\rangle$, $|\boldsymbol{p}'_A\boldsymbol{h}_B\rangle$, $|\boldsymbol{p}'_A\boldsymbol{h}'_B\rangle$, while in the second case it is expressed in the basis $|\boldsymbol{h}_A\boldsymbol{p}_B\rangle$, $|\boldsymbol{h}_A\boldsymbol{p}'_B\rangle$, $|\boldsymbol{h}'_A\boldsymbol{p}_B\rangle$, $|\boldsymbol{h}'_A\boldsymbol{p}'_B\rangle$. Imposing $\mathrm{Tr}(\rho) = 1$ yields in both cases $\eta^2 = 1/\cosh(\gamma)$. As is evident from Eqs. (11) and (12), the final state exhibits strong dependence on the order of the two elements and orientation of the corresponding eigenstates.

To quantify the degree of entanglement of the received state, we use concurrence as a figure of merit [42]. This can be extracted from the corresponding density matrices in the *filtering-first* and *decoherence-first* configurations, and the result, which follows after some cumbersome algebra, is in both cases

$$C = \frac{|R(\tau)|}{\cosh(\gamma)}. \tag{13}$$

Remarkably, unlike the shape of the state itself, the residual concurrence is not affected by any channel detail such as the relative orientation of the eigenstates of the two operators, or the order in which the two elements are concatenated. Instead it only depends on the channel's amount of filtering and magnitude of the birefringence vector. Our general result encompasses several previous findings. When decoherence acts alone ($\gamma = 0$), concurrence reduces to $C = |R(\tau)|$, which is the expression demonstrated in [35]. On the other hand, when decoherence is absent ($\tau = 0$), concurrence is given by $C = 1/\cosh(\gamma)$, as found in [36]. Finally, our result is consistent with the expression for concurrence found in [37], where the effect of mode-filtering on a Bell-diagonal state was studied. In what follows, we will provide a physical interpretation for the independence of concurrence on the order and relative orientation of the decoherence and filtering elements.

Filtering preceding decoherence. The way in which modal filtering in the A-optical path affects entanglement is through the probabilities of detecting specific two-photon polarization states (in the post-selected ensemble). If, prior to detection, the analyzer for photon A splits $\boldsymbol{h}_A$ and $\boldsymbol{h}'_A$, simultaneous clicks will be produced by the two states $|\boldsymbol{h}_A\boldsymbol{h}_B\rangle$ and $|\boldsymbol{h}'_A\boldsymbol{h}'_B\rangle$ only. However, if the analyzer splits a different pair of polarization states, say $\boldsymbol{p}_A$ and $\boldsymbol{p}'_A$, simultaneous clicks will be produced by the four states, $|\boldsymbol{p}_A\boldsymbol{h}_B\rangle$, $|\boldsymbol{p}'_A\boldsymbol{h}_B\rangle$, $|\boldsymbol{p}_A\boldsymbol{h}'_B\rangle$, and $|\boldsymbol{p}'_A\boldsymbol{h}'_B\rangle$, which emerge when expressing photon A in the basis $(\boldsymbol{p}_A, \boldsymbol{p}'_A)$. If $\boldsymbol{p}_A$ and $\boldsymbol{p}'_A$ happen to be aligned with the vector $\boldsymbol{\tau}$ defining a decoherence element concatenated to the mode-filtering element, then the temporal waveform associated with each of these four states does not suffer any distortion from decoherence (which simply introduces some delay in each of them); therefore, the corresponding probabilities of simultaneous clicks are not affected. This simple argument shows that the orientation of $\boldsymbol{\tau}$ does not interfere with the mechanism through which the preceding mode-filtering element affects the two-photon polarization entanglement.

Decoherence preceding filtering. The way in which decoherence in the A-optical path reduces entanglement is by correlating photon's A time of arrival with its polarization, so that in principle, one would be able to trace back the two photons' polarization based on their relative times of arrival. This ability is not affected by the presence of a mode-filtering element after decoherence in the path of photon A, as filtering does not distort the delayed replicas of the two-photon state waveform, but only the corresponding polarization contents, therefore leaving the arrival times of the two photons unchanged. This clarifies why the orientation of a decoherence element $\boldsymbol{\tau}$ preceding a mode-filtering element has no impact on concurrence.

The two arguments illustrated above also imply that the order in which the decohering and mode-filtering elements are concatenated cannot affect the two-photon polarization entanglement. In fact, as all possible relative orientations yield the same concurrence, all cases are equivalent to the one in which the vectors $\boldsymbol{\tau}$ and $\boldsymbol{\gamma}$ are aligned, and in this special case, the two effects commute with each other. Note that while concurrence is insensitive to the details of the two-element channel, the density matrices of the propagated state are not. The consequences of this on the design of a quantum network, such as choosing a direction in which the channel is to be used, are discussed in Sec. III.

III. EXPERIMENTAL VERIFICATION

In order to provide experimental evidence of the findings discussed in the previous section, we consider two different settings for both the *filtering-first* and *decoherence-first* configurations; one in which $\boldsymbol{\tau}$ and $\boldsymbol{\gamma}$ are aligned, and another in which they are orthogonal

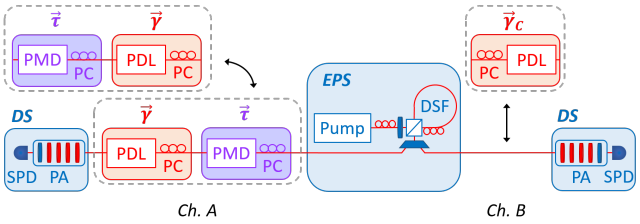

FIG. 1: Schematics of the experimental apparatus. $\boldsymbol{\tau}$: decohering element. $\boldsymbol{\gamma}$: filtering element. $\boldsymbol{\gamma}_C$: compensating filtering element. EPS: entangled photon source. DSF: dispersion-shifted fiber. PDL: PDL emulator. PMD: PMD emulator which applies a differential group delay $\tau = 6.6$ ps. PC: polarization controller. DS: detector station. PA: polarization analyzer consisting of several waveplates (red) and a polarizer (blue). SPD: single photon detector. The order of the decohering and filtering elements in channel A can be changed to investigate the *decoherence-first* and *filtering-first* cases.

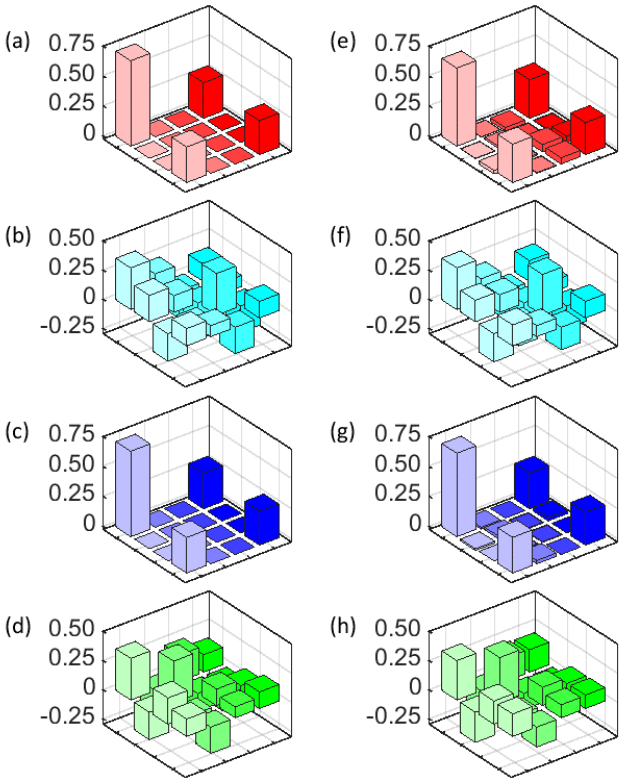

FIG. 2: Theoretical (left) and experimental (right) representation of Eqs.(11)-(12), for the case where the eigenvectors of the filtering and decoherence elements are aligned ((a)-(e) and (c)-(g)) and orthogonal ((b)-(f) and (d)-(h)) in Stokes space. The matrices in the top two rows ((a)-(b)-(e)-(f)) refer to the *filtering-first* scenario and are expressed in the basis $|\boldsymbol{p}_A\boldsymbol{h}_B\rangle$, $|\boldsymbol{p}_A\boldsymbol{h}'_B\rangle$, $|\boldsymbol{p}'_A\boldsymbol{h}_B\rangle$, $|\boldsymbol{p}'_A\boldsymbol{h}'_B\rangle$. The matrices in the bottom two rows ((c)-(g)-(d)-(h)) refer to the *decoherence-first* scenario and are expressed in the basis $|\boldsymbol{h}_A\boldsymbol{p}_B\rangle$, $|\boldsymbol{h}_A\boldsymbol{p}'_B\rangle$, $|\boldsymbol{h}'_A\boldsymbol{p}_B\rangle$, $|\boldsymbol{h}'_A\boldsymbol{p}'_B\rangle$. $\gamma = 0.46$ for all matrices.

to each other in Stokes space (or equivalently they form an angle of 45 degrees in Jones space). Our experimental setup consists of an entangled–photon source (EPS), telecom optical fibers, and two separate detector stations [43] that include polarization analyzers (PA) and InGaAs single photon detectors, which are used to perform state tomography [44]. In order to introduce controllable decoherence and modal filtering in the channel, we use polarization-mode dispersion (PMD) [40, 41] and polarization-dependent loss (PDL) [45, 46] emulators, respectively. The PDL emulators, which are fully configurable both in magnitude (within the 0 dB - 7 dB range) and orientation, can be inserted in the paths of the two photons. All of the PDL emulators are PMD-free, except for one that has a fixed differential group delay (DGD); we use the latter to reproduce the effect of lumped decoherence.

The entangled photons are generated inside the EPS by pumping a dispersion-shifted fiber (DSF) with a 50 MHz pulsed fiber laser that operates at 193.1 THz and creates signal and idler photons via four-wave mixing [47]. The average number of generated photon pairs per pulse can be tuned in the 0.001 – 0.1 range [48, 49]. The generated photons are spectrally separated and routed to channels on the 100 GHz-spaced ITU grid [50]. For this specific experiment, we use channels 28 (192.8 THz) and 34 (193.4 THz). The resulting photon temporal wavefunctions are of a sinc-like shape with temporal FWHM of about 15 ps. A relevant value of the fixed DGD of 6.6 ps was chosen to introduce a non-negligible entanglement reduction, corresponding to a concurrence of $C = 0.66$ in the absence of PDL [51]. A schematic of the experimental setup is shown in Fig. 1. The order of decoherence and modal filtering, as well as the relative orientation of $\boldsymbol{\tau}$ and $\boldsymbol{\gamma}$, can be varied to cover all of the possible configurations by adjusting the PMD and PDL emulators.

First, we experimentally confirm Eqs. (11, 12) in four specific cases. We introduce both a PDL and a PMD emulator in the channel of photon A and vary the emulators' order and orientation. That is, by using polarization controllers, we can either align vectors $\boldsymbol{\tau}$ and $\boldsymbol{\gamma}$ or make them orthogonal. The left column of Fig. 2 shows the matrices expressed by Eqs. (11, 12). The right column presents experimentally measured matrices in the same four scenarios. The two columns show striking similarities, thus verifying our theoretical calculations. Minor variations due to experimental noise are slightly noticeable in the zero-valued elements of the experimental matrices. The matrices in the top two rows, expressed in the basis $|\boldsymbol{p}_A\boldsymbol{h}_B\rangle$, $|\boldsymbol{p}_A\boldsymbol{h}'_B\rangle$, $|\boldsymbol{p}'_A\boldsymbol{h}_B\rangle$, $|\boldsymbol{p}'_A\boldsymbol{h}'_B\rangle$, correspond to the *filtering-first* scenario. Similarly, the bottom two rows of matrices refer to the *decoherence-first* configuration and are expressed in the basis $|\boldsymbol{h}_A\boldsymbol{p}_B\rangle$, $|\boldsymbol{h}_A\boldsymbol{p}'_B\rangle$, $|\boldsymbol{h}'_A\boldsymbol{p}_B\rangle$, $|\boldsymbol{h}'_A\boldsymbol{p}'_B\rangle$. The vectors $\boldsymbol{\tau}$ and $\boldsymbol{\gamma}$ are aligned for (a,c,e,g) and are orthogonal for (b,d,f,h). The four specific cases are color-coded in Fig. 2, and the same color coding is adopted throughout the rest of the paper. The figure clearly shows that the orientation and ordering of the decohering and filtering elements affect the final

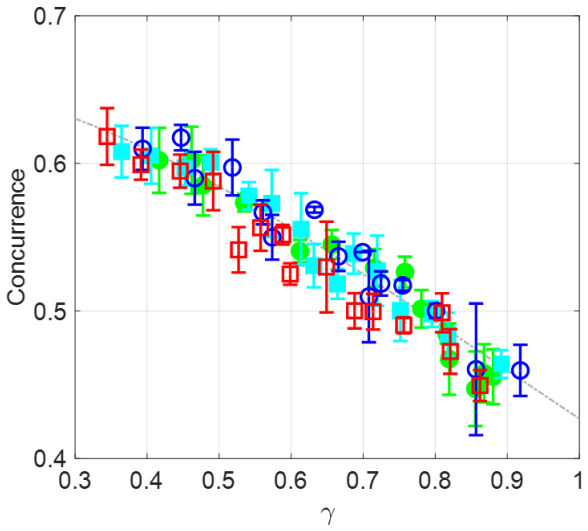

FIG. 3: Concurrence as a function of the amount of filtering γ in the channel. The dashed line represents the theoretical result Eq. (13). All of the markers are experimental points: squares refer to the *filtering-first* scenario, while circles refer to the *decoherence-first* scenario. In both cases, the empty markers correspond to the case in which the $\boldsymbol{\gamma}$ is aligned with $\boldsymbol{\tau}$, and the filled ones to the case in which they are orthogonal.

quantum state as seen in the different density matrices.

Next, we validate the theoretical expression Eq. (13), that is plotted in Fig. 3 with a dashed line. The symbols show the experimental concurrence as a function of the amount of filtering γ in the channel. The squares refer to the *filtering-first* configuration, and the circles refer to the *decoherence-first* scenario; empty and filled markers are used for the aligned and orthogonal configuration, respectively. All the data points are in excellent agreement with the theoretical curve. The plot confirms that the amount of entanglement is determined only by the magnitude of decoherence and the strength of the modal filtering and, contrary to the states themselves, is independent of either order or relative orientation.

Now we turn our attention to the ordering of the decohering and filtering elements, which is important in fiber channels for various reasons. A particularly illustrative case is the one with the decohering and filtering elements $\boldsymbol{\tau}$ and $\boldsymbol{\gamma}$ being orthogonal in Stokes space. Indeed in this case, if photon A is expressed in the basis $(\boldsymbol{h}_A, \boldsymbol{h}'_A)$, and photon B in the basis $(\boldsymbol{h}_B, \boldsymbol{h}'_B)$, the density matrix simplifies to

$$\rho_i = \frac{1}{4\cosh(\gamma)} \begin{pmatrix} e^{\gamma}(1+R(\tau)) & 0 & 0 & 1+R(\tau) \\ 0 & e^{\xi_i\gamma}(1-R(\tau)) & 1-R(\tau) & 0 \\ 0 & 1-R^*(\tau) & e^{-\xi_i\gamma}(1-R(\tau)) & 0 \\ 1+R^*(\tau) & 0 & 0 & e^{-\gamma}(1+R(\tau)) \end{pmatrix}, \tag{14}$$

where $i = 1$ and $i = 2$ correspond to the *filtering-first* and *decoherence-first* scenarios, respectively, and $\xi_1 = -\xi_2 = 1$. In this particularly illustrative situation, the two expressions can be obtained from each other by simply permutating the elements ρ_{22} and ρ_{33}. An experimental verification of this formula is presented in Fig. 4. The left panel shows experimental density matrices related to the two scenarios for $\gamma = 0.41, 0.66, 0.77$; the right panel shows a plot of the experimentally obtained coincidence probabilities given by the diagonal elements of ρ_i versus γ, with the four curves showing the corresponding theoretical expressions from Eq. (14). Consistent with the theory, one can see that as modal filtering in the channel is increased, $\rho_{i,11}$ increases and $\rho_{i,44}$ decreases, both in the *filtering-first* case (cyan markers), and in the *decoherence-first* scenario (green markers). On the other hand, in the *filtering-first* case, $\rho_{i,22}$ decreases with γ, and $\rho_{i,33}$ increases with it, whereas the opposite behaviour is observed in the *decoherence-first* scenario.

Our analysis shows that this simple difference between the two cases provides a powerful tool to gain information about the channel in which the photon is propagating when vector $\boldsymbol{\tau}$ and $\boldsymbol{\gamma}$ are orthogonal in Stokes space. By simply measuring ρ_{22} and ρ_{33}, that is by recording only coincidence counts along $(\boldsymbol{h}_A, \boldsymbol{h}'_B)$ and $(\boldsymbol{h}'_A, \boldsymbol{h}_B)$ instead of reconstructing the whole density matrix, one can in fact tell whether modal loss or decoherence comes first. Note that ρ_{22} and ρ_{33} are indicative of the quantum bit error ratio (QBER), and nearly all quantum protocols monitor QBER on a regular basis.

The knowledge of whether filtering is concentrated toward the beginning or the end of a long optical route is very important for Procrustean entanglement distillation [52–54], as we illustrate with our two-element model of Eqs. (11, 12) below. It has been shown that a judicially selected pair of filters could distill entanglement from certain mixed states [55–58]. More recently, our group investigated how a filter applied to photon B of an entangled pair could partially or fully restore entanglement diminished by inadvertent filtering inherent to channel A. We previously found that when the filtering is concentrated towards the end of the route, a situation that corresponds to the *decoherence-first* case of our model, the entanglement could be restored fully or partially depending on the type of noise encountered by photon A [36–38].

For the opposite case of the *filtering-first* scenario in

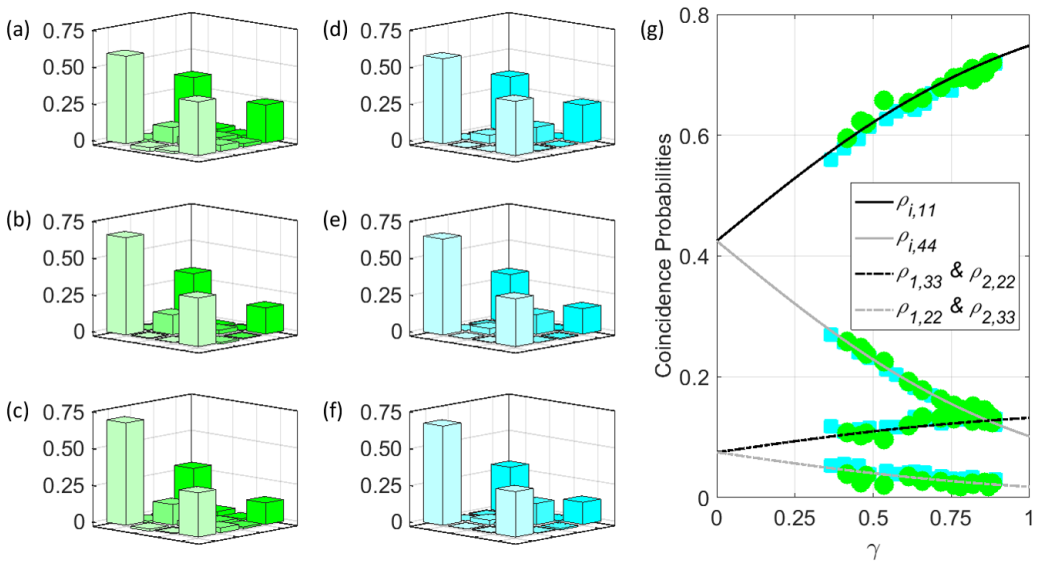

FIG. 4: Experimental results of the setup reproducing Eq. (14) for the *decoherence-first* (green) and *filtering-first* (cyan) cases when $\boldsymbol{\tau}$ and $\boldsymbol{\gamma}$ are orthogonal in Stokes space. Left panel: experimental density matrices expressed in the basis $|\boldsymbol{h}_A\boldsymbol{h}_B\rangle$, $|\boldsymbol{h}_A\boldsymbol{h}'_B\rangle$, $|\boldsymbol{h}'_A\boldsymbol{h}_B\rangle$, $|\boldsymbol{h}'_A\boldsymbol{h}'_B\rangle$, for $\gamma = 0.41$ (a, d), 0.66 (b, e), and 0.77 (c, f). Right panel: coincidence probabilities, measured via the diagonal elements of the density matrix, as a function of γ. Comparison of $\rho_{i,11}$, $\rho_{i,22}$, $\rho_{i,33}$, and $\rho_{i,44}$, where $i = 1, 2$ for the *filtering-first* and *decoherence-first* cases, respectively. $\rho_{i,11}$ and $\rho_{i,44}$ are independent of the ordering of the two effects; however, $\rho_{1,22}$ is equivalent to $\rho_{2,33}$, and vice-versa.

channel A, distillation with the help of an additional filter in channel B is rather straightforward [59], and we demonstrate it below for the sake of completeness. Figure 5 plots concurrence as a function of increasing γ for the *filtering-first* case. A fixed decoherence element follows the filter in channel A and is responsible for the decreased concurrence of $C = 0.66$ for $\gamma = 0$. Color-coded filled and empty symbols correspond to aligned and orthogonal $\boldsymbol{\tau}$ and $\boldsymbol{\gamma}$, respectively. The dashed curve is a plot of Eq. (13). The upper set of data points demonstrates entanglement restoration when an extra filter is added to channel B. The solid curve shows the restored concurrence value, also given by the same equation with $\gamma = 0$, that is, the value that would be observed if only the decohering element were present in the optical path of photon A [35]. The data points show that full compensation can be achieved for all filtering levels regardless of the relative orientation of $\boldsymbol{\tau}$ and $\boldsymbol{\gamma}$.

To conclude this section, we note that the greater effectiveness of nonlocal compensation in the *filtering-first* configuration relative to the *decoherence-first* configuration demonstrated above has important implications in the design of optical networks for polarization-entanglement distribution. Indeed, the same channel could in general be used for photon distribution in two opposite directions, as could be the case for a specific graph edge of a quantum network, or when two parties take turns in exchanging messages using a point-to-point connection. Either way, the resulting channel will cause different impairments depending on the photon's propagation direction [60].

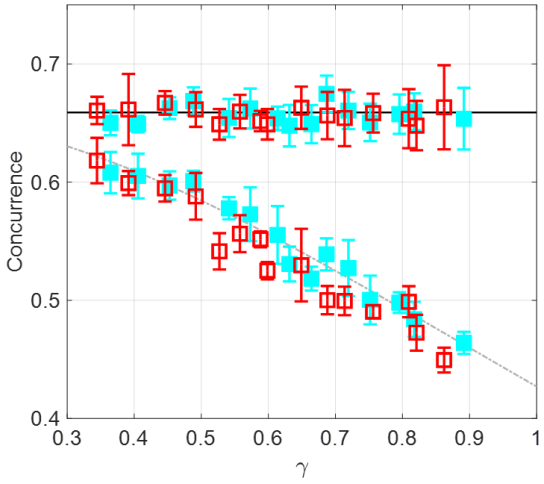

FIG. 5: Concurrence versus the filtering magnitude γ in the *filtering-first* scenario. Empty and filled markers correspond to the cases in which the vectors $\boldsymbol{\gamma}$ and $\boldsymbol{\tau}$ are aligned and orthogonal, respectively. The upper set of data points refer to the case in which nonlocal compensation of modal filtering is implemented by passing photon B through and additional filtering element. The dashed curve is the analytical result Eq. (13) and the solid curve shows the restored concurrence level, also given by the same equation with $\gamma = 0$.

IV. RELATION TO A GENERAL FIBER-OPTIC CHANNEL

In this section, we expand our treatment of a bi-photon quantum state, one photon of which is distributed over an optical fiber, to include a more general channel model. In Sections II and III, the channel was represented by two lumped elements, the order and relative orientation of which we had carefully examined. Installed fibers and free space channels are naturally more complex because the optical path is long and perturbations that cause decoherence and mode filtering are local in nature, numerous, and occur throughout the length of the route [40, 46, 61–64]. PMD serves as a major source of decoherence for polarization entanglement [33–35], while filtering arises from PDL [36–38]. Since PMD and PDL originate from spatially distributed sources, their effect is not simply that of two lumped sources; instead, they add in a rather complex fashion. However, their joint effect on a sufficiently narrow-band signal can be described by the following frequency-dependent transfer matrix [65]:

$$\mathbf{T}(\omega) = \exp\left(-\frac{i}{2}\omega\tilde{\boldsymbol{\tau}}\cdot\boldsymbol{\sigma}\right)\mathbf{T}_0, \tag{15}$$

where $\mathbf{T}_0$ is the transfer matrix at $\omega = 0$ and can be assumed to be in the diagonal form of Eq. (6) with no loss of generality. The symbol $\tilde{\boldsymbol{\tau}}$ denotes a three-dimensional vector. By letting the components of $\tilde{\boldsymbol{\tau}}$ be complex-valued, Eq. (15) describes the most general channel instantiation. In this case, the imaginary component of $\tilde{\boldsymbol{\tau}}$ is responsible for the presence of frequency-dependent PDL, which has non-trivial implications in terms of waveform distortion [65].

If photon A of the polarization-entangled state in Eq. (4) propagates in a fiber link described by Eq. (15), and photon B does not suffer any propagation effects, the received two-photon state can be expressed as

$$|\psi_{\text{out}}\rangle = \eta \int\int d\omega_A d\omega_B \tilde{f}(\omega_A,\omega_B)|\omega_A,\omega_B\rangle \otimes \frac{|\mathbf{T}(\omega_A)\boldsymbol{h}_A,\boldsymbol{h}_B\rangle + |\mathbf{T}(\omega_A)\boldsymbol{h}'_A,\boldsymbol{h}'_B\rangle}{\sqrt{2}}, \tag{16}$$

where the coefficient η ensures that the output state is correctly normalized after post-selection. The density matrix ρ characterizing the polarization properties of the received state is then obtained by tracing the full density matrix $|\psi_{\text{out}}\rangle\langle\psi_{\text{out}}|$ over the frequency modes:

$$\rho_{ij} = \frac{\eta^2}{2}\int\int d\omega_A d\omega_B |f(\omega_A,\omega_B)|^2 T_{n_i,m_i}(\omega_A)T^*_{n_j,m_j}(\omega_A), \tag{17}$$

where T_{n_i,m_j} denotes the element (n_i,m_j) of $\mathbf{T}$, with $n_1 = n_2 = 1$, $n_3 = n_4 = 2$, $m_1 = m_3 = 1$, and $m_2 = m_4 = 2$, whose computation is more convenient using the following expansion:

$$\exp\left(\frac{i}{2}\omega\tilde{\boldsymbol{\tau}}\cdot\boldsymbol{\sigma}\right) = \cos\left(\frac{\omega\tilde{\tau}}{2}\right)\mathbf{I} - i\frac{\tilde{\boldsymbol{\tau}}\cdot\boldsymbol{\sigma}}{\tilde{\tau}}\sin\left(\frac{\omega\tilde{\tau}}{2}\right), \tag{18}$$

where $\tilde{\tau}$ is either one of the square roots of $\tilde{\boldsymbol{\tau}}\cdot\tilde{\boldsymbol{\tau}}$.

Since the simple analytical two-element model of Eqs. (11, 12) must be a particular case of the general channel description of Eq. (17), we begin by finding the constraints that reduce the latter to the former. Clearly, a real-valued vector $\tilde{\boldsymbol{\tau}}$, such that $\tilde{\boldsymbol{\tau}} = \boldsymbol{\tau}$, reduces the general channel to the *filtering-first* configuration. On the other hand, the constraints for the *decoherence-first* configuration are a bit more involved. This configuration is characterized by the transfer matrix

$$\mathbf{T}(\omega) = \mathbf{T}_0\exp\left(-\frac{i}{2}\omega\boldsymbol{\tau}\cdot\boldsymbol{\sigma}\right) = \exp\left(-\frac{i}{2}\omega\tilde{\boldsymbol{\tau}}\cdot\boldsymbol{\sigma}\right)\mathbf{T}_0, \tag{19}$$

where the second equality implies the identity $\tilde{\boldsymbol{\tau}}\cdot\boldsymbol{\sigma} = \mathbf{T}_0\boldsymbol{\tau}\cdot\boldsymbol{\sigma}\mathbf{T}_0^{-1}$, which yields

$$\tilde{\tau}_1 = \tau_1 \tag{20}$$

$$\tilde{\tau}_2 = \cosh(\gamma)\tau_2 - i\sinh(\gamma)\tau_3 \tag{21}$$

$$\tilde{\tau}_3 = \cosh(\gamma)\tau_3 + i\sinh(\gamma)\tau_2. \tag{22}$$

Inspection of Eqs. (20–22) shows that the real and imaginary components of the complex vector $\tilde{\boldsymbol{\tau}}$, which we denote by $\tilde{\boldsymbol{\tau}}_R$ and $\tilde{\boldsymbol{\tau}}_I$, respectively, are orthogonal to each other. This constitutes the most relevant feature of the manifold of complex vectors $\tilde{\boldsymbol{\tau}}$ spanned by the *decoherence-first* configuration.

Another, less restrictive, implication of Eqs. (20–22) is that the square length of the real component of $\tilde{\boldsymbol{\tau}}$ exceeds that of its imaginary component by the square length of $\boldsymbol{\tau}$, namely by the square differential group delay of the corresponding PDL-free link ($|\tilde{\boldsymbol{\tau}}_R|^2 - |\tilde{\boldsymbol{\tau}}_I|^2 = \tau^2$). Both of these relations emerge *on average* in all fiber-optic links [65], including space-division multiplexed transmission links based on multi-core and multi-mode fibers [66], where the complex vector $\tilde{\boldsymbol{\tau}}$ is a random quantity. In particular, denoting by $\mathbb{E}$ ensemble averaging, the analogue of the first relation is $\mathbb{E}[\tilde{\boldsymbol{\tau}}_R\cdot\tilde{\boldsymbol{\tau}}_I] = 0$, while the analogue of the second is $\mathbb{E}[|\tilde{\boldsymbol{\tau}}_R|^2] - \mathbb{E}[|\tilde{\boldsymbol{\tau}}_I|^2] = \mathbb{E}[\tau^2]$, where $\mathbb{E}[\tau^2]$ is intended to be the mean-square DGD that would accumulate in the link if PDL were absent. The latter relation does not ensure that the inequality $|\tilde{\boldsymbol{\tau}}_R| \geq |\tilde{\boldsymbol{\tau}}_I|$ is always fulfilled, but it does imply that its violation occurs with low probability. This primarily occurs for unrealistically large PDL values [65], which makes it of little relevance. Finally, it is worth noting that even if $|\boldsymbol{\tau}_R| \geq |\boldsymbol{\tau}_I|$, Eqs. (20–22) do not ensure that any arbitrary value of $|\boldsymbol{\tau}_R|$ and $|\boldsymbol{\tau}_I|$ can be matched. Indeed, for a given instance of $|\boldsymbol{\tau}_R|$ and $|\boldsymbol{\tau}_I|$, the values of τ_1, τ_2, and τ_3 must satisfy the relation

$$\frac{\tau_2^2+\tau_3^2}{\tau_1^2+\tau_2^2+\tau_3^2} = \frac{1}{(|\tilde{\boldsymbol{\tau}}_R|^2/|\tilde{\boldsymbol{\tau}}_I|^2 - 1)\sinh^2(\gamma)} \leq 1, \tag{23}$$

where $\tau_1^2+\tau_2^2+\tau_3^2 = \tau^2 = |\tilde{\boldsymbol{\tau}}_R|^2 - |\tilde{\boldsymbol{\tau}}_I|^2$, and where γ is dictated by $\mathbf{T}_0$. Clearly, specific combinations of values of $|\boldsymbol{\tau}_R|$, $|\boldsymbol{\tau}_I|$, and γ can violate the inequality in Eq. (23).

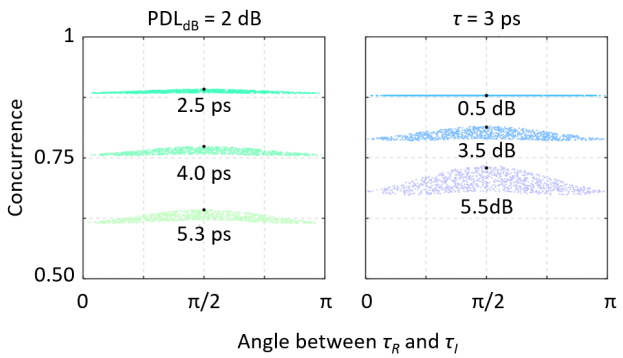

FIG. 6: Concurrence as a function of the angle formed by the real and imaginary parts of the complex-valued vector $\tilde{\boldsymbol{\tau}} = \tilde{\boldsymbol{\tau}}_R + i\tilde{\boldsymbol{\tau}}_I$. The larger black dots refer to the *decoherence-first* configuration, where the vector $\tilde{\boldsymbol{\tau}}$ is given by Eqs. (20–22), while the smaller dots were obtained by randomly varying the orientation of the real and imaginary parts of the same vector.

As an aside, this limitation disappears in a lumped element channel with an additional PDL element, so that the three-element channel is $\mathbf{T}_1 \exp(i\omega\boldsymbol{\tau}\cdot\boldsymbol{\sigma}/2)\mathbf{T}_2 = \exp(i\omega\tilde{\boldsymbol{\tau}}\cdot\boldsymbol{\sigma}/2)\mathbf{T}_1\mathbf{T}_2$, with $\mathbf{T}_1\mathbf{T}_2 = \mathbf{T}_0$. Here, the coefficient γ_1 of $\mathbf{T}_1$ provides an additional degree of freedom in Eq. (23), which decouples the problem of matching $|\boldsymbol{\tau}_R|$ and $|\boldsymbol{\tau}_I|$ from that of matching $\mathbf{T}_0$.

In what follows, we compare the simple two-element channel model we proposed in Sec. II to the most general polarization channel. We argue that while the latter precisely reproduces the real channel, the former captures its main characteristics over a pertinent range of the channel parameters with sufficient accuracy. To this end, we investigate the effect of the relative orientation of $\tilde{\boldsymbol{\tau}}_R$ and $\tilde{\boldsymbol{\tau}}_I$ on the degree of entanglement of the received two-photon state. For a meaningful comparison, we start from the *decoherence-first* configuration of Eq. (19), with some fixed value of γ and τ (as discussed in Sect. II, the orientation of the decoherence vector $\boldsymbol{\tau}$ is immaterial in this context). We then evaluate the corresponding complex vector $\tilde{\boldsymbol{\tau}}$ according to Eqs. (20–22) and randomly vary the orientation of its real and imaginary components while keeping their lengths fixed. For each instance of $\tilde{\boldsymbol{\tau}}$, we evaluate the reduced density matrix ρ of the propagated two-photon state and extract the corresponding concurrence C [42].

The results are shown in Fig. 6, where concurrence is plotted as a function of the angle formed by the real and imaginary components of $\tilde{\boldsymbol{\tau}}$. The data points in the left panel were obtained for the displayed values of the DGD τ and for $\gamma = 0.23$, which corresponds to a PDL value in decibel [67] of $\mathrm{PDL_{dB}} = 2$ dB. The data points in the right panel were obtained for values of γ corresponding to the displayed values of $\mathrm{PDL_{dB}}$ and for a DGD of 3 ps. In this example, we assume a super-Gaussian profile of third order for both the pump power spectrum $|\tilde{E}_p(\omega)|^2$ and the filters' transmittivities $|H_{A,B}(\omega)|^2$ (Eq. (3)). For the former, we use a 3-dB bandwidth of 50 GHz, while for the latter, we use a 3-dB bandwidth of 100 GHz. The figure shows that varying the orientation of $\tilde{\boldsymbol{\tau}}_R$ and $\tilde{\boldsymbol{\tau}}_I$ produces some scattering of the measured concurrence below the *decoherence-first* configuration value, which is shown with the bigger dot. Extensive simulations show that this scattering is mostly affected by the magnitude of PDL, but it remains almost negligible for PDL and DGD values of practical relevance. Therefore, the *decoherence-first* case serves as a reliable tool for assessing entanglement degradation over a general channel.

As a final remark, we note the symmetry between the *decoherence-first* and *filtering-first* scenarios. Indeed, Eq. (15) could be easily rearranged in the following form:

$$\mathbf{T}(\omega) = \exp\left(-\frac{i}{2}\omega\tilde{\boldsymbol{\tau}}\cdot\boldsymbol{\sigma}\right)\mathbf{T}_0 = \mathbf{T}_0\exp\left(-\frac{i}{2}\omega\tilde{\boldsymbol{\tau}}'\cdot\boldsymbol{\sigma}\right), \tag{24}$$

where the complex-valued vector $\tilde{\boldsymbol{\tau}}'$ is defined through the relation $\tilde{\boldsymbol{\tau}}'\cdot\boldsymbol{\sigma} = \boldsymbol{T}_0^{-1}\tilde{\boldsymbol{\tau}}'\cdot\boldsymbol{\sigma}\boldsymbol{T}_0$. For the general channel, the constraints on the complex-valued vector $\tilde{\boldsymbol{\tau}}$ will reverse between the *filtering-first* and *decoherence-first* configurations. Correspondingly, our modelling results then reflect the *filtering-first* scenario. Hence, the two configurations are equally capable of emulating a general fiber-optic channel.

V. CONCLUSION

To gain insights into fiber-optic quantum channels, we studied a quantum channel with decoherence and mode filtering acting on one photon of a travelling EPR pair. First, we devised an analytical channel model for the case of two lumped elements, one causing decoherence and another causing partial mode filtering, and we derived analytical expressions for the density matrices of the propagated bi-photon states, as well as for their concurrence. The model permits us to examine the effect of the relative Bloch sphere orientation and the order in which a photon encounters the two elements, a reality in fiber-optic channels, where changes in ambient conditions dynamically reorient various polarization elements along the light-path. We verified these findings in four specific experimental scenarios and proposed a method of channel characterization via QBER measurements. Interestingly, while the output quantum states depend on these channel characteristics, the amount of entanglement quantified by concurrence does not. We further checked the ability of our two-element model to describe the most general fiber-optic channel, where the effect of a multitude of small arbitrarily oriented decoherence and mode-filtering elements accumulates along the optical path. This corresponds to the most relevant case of polarization entanglement distribution in fiber-optic networks. By numerically investigating the effect of such a general channel, we established a wide parameter

range where our analytical two-element model serves as an accurate approximation of the general channel. These results offer an elegant tool to develop an intuition into fiber quantum channels and, hence, pave the way for future quantum telecommunication.

ACKNOWLEDGMENTS

Work supported by US Research Army Lab through Grant W911NF1820155. G. Riccardi and C. Antonelli also acknowledge financial support from the Italian Government through Projects INCIPICT and PRIN2017 FIRST.

[1] B. A. Bell, D. Markham, D. A. Herrera-Martí, A. Marin, W. J. Wadsworth, J. G. Rarity, and M. S. Tame, Experimental demonstration of graph-state quantum secret sharing, Nature Communications **5**, 5480 (2014).

[2] M. de Oliveira, I. Nape, J. Pinnell, N. TabeBordbar, and A. Forbes, Experimental high-dimensional quantum secret sharing with spin-orbit-structured photons, Phys. Rev. A **101**, 042303 (2020).

[3] Y. Ding, D. Bacco, K. Dalgaard, X. Cai, X. Zhou, K. Rottwitt, and L. K. Oxenløwe, High-dimensional quantum key distribution based on multicore fiber using silicon photonic integrated circuits, npj Quantum Information **3**, 25 (2017).

[4] G. L. Roberts, M. Lucamarini, Z. L. Yuan, J. F. Dynes, L. C. Comandar, A. W. Sharpe, A. J. Shields, M. Curty, I. V. Puthoor, and E. Andersson, Experimental measurement-device-independent quantum digital signatures, Nature Communications **8**, 1098 (2017).

[5] K. Wang, X. Wang, X. Zhan, Z. Bian, J. Li, B. C. Sanders, and P. Xue, Entanglement-enhanced quantum metrology in a noisy environment, Phys. Rev. A **97**, 042112 (2018).

[6] H. Shi, Z. Zhang, and Q. Zhuang, Practical route to entanglement-assisted communication over noisy bosonic channels, Phys. Rev. Applied **13**, 034029 (2020).

[7] S. Ray, J. Schneeloch, C. C. Tison, and P. M. Alsing, Maximum advantage of quantum illumination, Phys. Rev. A **100**, 012327 (2019).

[8] M. F. Sacchi and T. Sacchi, Convex approximations of quantum channels, Phys. Rev. A **96**, 032311 (2017).

[9] T. P. W. Cope, L. Hetzel, L. Banchi, and S. Pirandola, Simulation of non-pauli channels, Phys. Rev. A **96**, 022323 (2017).

[10] J. ur Rehman, Y. Jeong, and H. Shin, Directly estimating the holevo capacity of discrete weyl channels, Phys. Rev. A **99**, 042312 (2019).

[11] M. M. Wilde, Entanglement cost and quantum channel simulation, Phys. Rev. A **98**, 042338 (2018).

[12] J.-S. Xu, M.-H. Yung, X.-Y. Xu, J.-S. Tang, C.-F. Li, and G.-C. Guo, Robust bidirectional links for photonic quantum networks, Science Advances **2**, 10.1126/sciadv.1500672 (2016).

[13] W.-K. Mok, D. Aghamalyan, J.-B. You, T. Haug, W. Zhang, C. E. Png, and L.-C. Kwek, Long-distance dissipation-assisted transport of entangled states via a chiral waveguide, Phys. Rev. Research **2**, 013369 (2020).

[14] D. Cozzolino, D. Bacco, B. Da Lio, K. Ingerslev, Y. Ding, K. Dalgaard, P. Kristensen, M. Galili, K. Rottwitt, S. Ramachandran, and L. K. Oxenløwe, Orbital angular momentum states enabling fiber-based high-dimensional quantum communication, Phys. Rev. Applied **11**, 064058 (2019).

[15] J. Liu, I. Nape, Q. Wang, A. Vallés, J. Wang, and A. Forbes, Multidimensional entanglement transport through single-mode fiber, Science Advances **6**, 10.1126/sciadv.aay0837 (2020).

[16] Y.-L. Tang, H.-L. Yin, Q. Zhao, H. Liu, X.-X. Sun, M.-Q. Huang, W.-J. Zhang, S.-J. Chen, L. Zhang, L.-X. You, Z. Wang, Y. Liu, C.-Y. Lu, X. Jiang, X. Ma, Q. Zhang, T.-Y. Chen, and J.-W. Pan, Measurement-device-independent quantum key distribution over untrustful metropolitan network, Phys. Rev. X **6**, 011024 (2016).

[17] R. Valivarthi, M. G. Puigibert, Q. Zhou, G. H. Aguilar, V. B. Verma, F. Marsili, M. D. Shaw, S. W. Nam, D. Oblak, and W. Tittel, Quantum teleportation across a metropolitan fibre network, Nature Photonics **10**, 676 (2016).

[18] A. Boaron, G. Boso, D. Rusca, C. Vulliez, C. Autebert, M. Caloz, M. Perrenoud, G. Gras, F. Bussières, M.-J. Li, D. Nolan, A. Martin, and H. Zbinden, Secure quantum key distribution over 421 km of optical fiber, Phys. Rev. Lett. **121**, 190502 (2018).

[19] X.-T. Fang, P. Zeng, H. Liu, M. Zou, W. Wu, Y.-L. Tang, Y.-J. Sheng, Y. Xiang, W. Zhang, H. Li, Z. Wang, L. You, M.-J. Li, H. Chen, Y.-A. Chen, Q. Zhang, C.-Z. Peng, X. Ma, T.-Y. Chen, and J.-W. Pan, Implementation of quantum key distribution surpassing the linear rate-transmittance bound, Nature Photonics **14**, 422 (2020).

[20] J.-G. Ren, P. Xu, H.-L. Yong, L. Zhang, S.-K. Liao, J. Yin, W.-Y. Liu, W.-Q. Cai, M. Yang, L. Li, K.-X. Yang, X. Han, Y.-Q. Yao, J. Li, H.-Y. Wu, S. Wan, L. Liu, D.-Q. Liu, Y.-W. Kuang, Z.-P. He, P. Shang, C. Guo, R.-H. Zheng, K. Tian, Z.-C. Zhu, N.-L. Liu, C.-Y. Lu, R. Shu, Y.-A. Chen, C.-Z. Peng, J.-Y. Wang, and J.-W. Pan, Ground-to-satellite quantum teleportation, Nature **549**, 70 (2017).

[21] S. Wengerowsky, S. K. Joshi, F. Steinlechner, J. R. Zichi, S. M. Dobrovolskiy, R. van der Molen, J. W. N. Los, V. Zwiller, M. A. M. Versteegh, A. Mura, D. Calonico, M. Inguscio, H. Hübel, L. Bo, T. Scheidl, A. Zeilinger, A. Xuereb, and R. Ursin, Entanglement distribution over a 96-km-long submarine optical fiber, Proceedings of the National Academy of Sciences **116**, 6684 (2019), https://www.pnas.org/content/116/14/6684.full.pdf.

[22] S. Wengerowsky, S. K. Joshi, F. Steinlechner, J. R. Zichi, B. Liu, T. Scheidl, S. M. Dobrovolskiy, R. v. d. Molen, J. W. N. Los, V. Zwiller, M. A. M. Versteegh, A. Mura, D. Calonico, M. Inguscio, A. Zeilinger, A. Xuereb, and R. Ursin, Passively stable distribution of polarisation entanglement over 192 km of deployed optical fibre, npj

Quantum Information **6**, 5 (2020).
[23] C. M. Mabena and F. S. Roux, High-dimensional quantum channel estimation using classical light, Phys. Rev. A **96**, 053860 (2017).
[24] A. Z. Goldberg, Quantum theory of polarimetry: From quantum operations to mueller matrices, Phys. Rev. Research **2**, 023038 (2020).
[25] Y. Mao, Y.-Z. Zhen, H. Liu, M. Zou, Q.-J. Tang, S.-J. Zhang, J. Wang, H. Liang, W. Zhang, H. Li, L. You, Z. Wang, L. Li, N.-L. Liu, K. Chen, T.-Y. Chen, and J.-W. Pan, Experimentally verified approach to nonentanglement-breaking channel certification, Phys. Rev. Lett. **124**, 010502 (2020).
[26] F. Graffitti, A. Pickston, P. Barrow, M. Proietti, D. Kundys, D. Rosset, M. Ringbauer, and A. Fedrizzi, Measurement-device-independent verification of quantum channels, Phys. Rev. Lett. **124**, 010503 (2020).
[27] M. K. Gupta and J. P. Dowling, Dephasing of single-photon orbital angular momentum qudit states in fiber: Limits to correction via dynamical decoupling, Phys. Rev. Applied **5**, 064013 (2016).
[28] Y.-Y. Ding, H. Chen, S. Wang, D.-Y. He, Z.-Q. Yin, W. Chen, Z. Zhou, G.-C. Guo, and Z.-F. Han, Polarization variations in installed fibers and their influence on quantum key distribution systems, Opt. Express **25**, 27923 (2017).
[29] D. Vasylyev, A. A. Semenov, and W. Vogel, Atmospheric quantum channels with weak and strong turbulence, Phys. Rev. Lett. **117**, 090501 (2016).
[30] D. Vasylyev, W. Vogel, and A. A. Semenov, Theory of atmospheric quantum channels based on the law of total probability, Phys. Rev. A **97**, 063852 (2018).
[31] S. Wang, P. Huang, T. Wang, and G. Zeng, Feasibility of all-day quantum communication with coherent detection, Phys. Rev. Applied **12**, 024041 (2019).
[32] G. Stein, V. Bushmakin, Y. Wang, A. W. Schell, and I. Gerhardt, Narrow-band fiber-coupled single-photon source, Phys. Rev. Applied **13**, 054042 (2020).
[33] C. Antonelli, M. Shtaif, and M. Brodsky, Sudden death of entanglement induced by polarization mode dispersion, Phys. Rev. Lett. **106**, 080404 (2011).
[34] M. Shtaif, C. Antonelli, and M. Brodsky, Nonlocal compensation of polarization mode dispersion in the transmission of polarization entangled photons, Opt. Express **19**, 1728 (2011).
[35] M. Brodsky, E. C. George, C. Antonelli, and M. Shtaif, Loss of polarization entanglement in a fiber-optic system with polarization mode dispersion in one optical path, Opt. Lett. **36**, 43 (2011).
[36] D. E. Jones, B. T. Kirby, and M. Brodsky, Tuning quantum channels to maximize polarization entanglement for telecom photon pairs, npj Quantum Inf. **4**, 58 (2018).
[37] B. T. Kirby, D. E. Jones, and M. Brodsky, Effect of polarization dependent loss on the quality of transmitted polarization entanglement, J. Light. Technol. **37**, 95 (2019).
[38] D. E. Jones, B. T. Kirby, G. Riccardi, C. Antonelli, and M. Brodsky, Exploring classical correlations in noise to recover quantum information using local filtering, New Journal of Physics **22**, 073037 (2020).
[39] M. Brodsky, N. J. Frigo, M. Boroditsky, and M. Tur, Polarization mode dispersion of installed fibers, J. Lightwave Technol. **24**, 4584 (2006).
[40] M. Brodsky, N. J. Frigo, and M. Tur, Polarization mode dispersion, in *Optical Fiber Telecommunications A*, Optics and Photonics, edited by I. P. Kaminow, T. Li, and A. E. Willner (Academic Press, Burlington, 2008) 5th ed., pp. 605 – 669.
[41] J. Gordon and H. Kogelnik, Pmd fundamentals: Polarization mode dispersion in optical fibers, Proc. Natl. Acad. Sci. **97**, 4541 (2000).
[42] W. K. Wootters, Entanglement of formation of an arbitrary state of two qubits, Phys. Rev. Lett. **80**, 2245 (1998).
[43] NuCrypt, Quantum optical instrumentation.
[44] J. B. Altepeter, E. R. Jeffrey, and P. G. Kwiat, Photonic state tomography, Adv. Atom. Mol. Opt. Phys. **52**, 105 (2005).
[45] N. Gisin, Statistics of polarization dependent losses, Opt. Commun. **114**, 399 (1995).
[46] O. Liboiron-Ladouceur, K. Bergman, M. Boroditsky, and M. Brodsky, Polarization-dependent gain in soa-based optical multistage interconnection networks, J. Light. Technol. **24**, 3959 (2006).
[47] M. Fiorentino, P. L. Voss, J. E. Sharping, and P. Kumar, All-fiber photon-pair source for quantum communications, IEEE Photonics Technol. Lett. **14**, 983 (2002).
[48] D. E. Jones, B. T. Kirby, and M. Brodsky, Joint characterization of two single photon detectors with a fiber-based source of entangled photon pairs, in *Frontiers in Opt.* (Opt. Soc. of America, 2017) pp. JW4A–37.
[49] D. E. Jones, B. T. Kirby, and M. Brodsky, In-situ calibration of fiber-optics entangled photon distribution system, in *IEEE Photonics Soc. Summer Topical Meeting Ser.* (IEEE, 2017) pp. 123–124.
[50] S. X. Wang and G. S. Kanter, Robust multiwavelength all-fiber source of polarization-entangled photons with built-in analyzer alignment signal, IEEE J. Sel. Top. Quantum Electron. **15**, 1733 (2009).
[51] In general for these temporal waveforms, a drop of concurrence from 1 to 0 can be seen by increasing the DGD from 0 to 14 ps, as shown in Fig. 2 of [35].
[52] A. Kent, N. Linden, and S. Massar, Optimal entanglement enhancement for mixed states, Phys. Rev. Lett. **83**, 2656 (1999).
[53] N. Linden, S. Massar, and S. Popescu, Purifying noisy entanglement requires collective measurements, Phys. Rev. Lett. **81**, 3279 (1998).
[54] F. Verstraete, J. Dehaene, and B. DeMoor, Local filtering operations on two qubits, Phys. Rev. A **64**, 010101 (2001).
[55] P. G. Kwiat, S. Barraza-Lopez, A. Stefanov, and N. Gisin, Experimental entanglement distillation and 'hidden'non-locality, Nature **409**, 1014 (2001).
[56] Z.-W. Wang, X.-F. Zhou, Y.-F. Huang, Y.-S. Zhang, X.-F. Ren, and G.-C. Guo, Experimental entanglement distillation of two-qubit mixed states under local operations, Phys. Rev. Lett. **96**, 220505 (2006).
[57] R. T. Thew and W. J. Munro, Entanglement manipulation and concentration, Phys. Rev. A **63**, 030302 (2001).
[58] R. T. Thew and W. J. Munro, Mixed state entanglement: Manipulating polarization-entangled photons, Phys. Rev. A **64**, 022320 (2001).
[59] B. T. Kirby, personal communication (2019).
[60] G. Riccardi, D. E. Jones, C. Antonelli, and M. Brodsky, Directional asymmetry of quantum channels, in *Frontiers in Optics + Laser Science APS/DLS* (Optical Society of America, 2020) p. FM1C.1.

[61] M. Boroditsky, M. Brodsky, N. J. Frigo, P. Magill, and L. Raddatz, In-service measurements of polarization-mode dispersion and correlation to bit-error rate, IEEE Photonics Technology Letters **15**, 572 (2003).

[62] A. Mecozzi, C. Antonelli, M. Boroditsky, and M. Brodsky, Characterization of the time dependence of polarization mode dispersion, Opt. Lett. **29**, 2599 (2004).

[63] C. Antonelli, A. Mecozzi, K. Cornick, M. Brodsky, and M. Boroditsky, Pmd-induced penalty statistics in fiber links, IEEE Photonics Technology Letters **17**, 1013 (2005).

[64] M. Brodsky, M. Boroditsky, P. Magill, N. Frigo, and M. Tur, Persistence of spectral variations in dgd statistics, Opt. Express **13**, 4090 (2005).

[65] M. Shtaif and O. Rosenberg, Polarization-dependent loss as a waveform-distorting mechanism and its effect on fiber-optic systems, J. Light. Technol. **23**, 923 (2005).

[66] C. Antonelli, A. Mecozzi, M. Shtaif, N. K. Fontaine, H. Chen, and R. Ryf, Stokes-space analysis of modal dispersion of sdm fibers with mode-dependent loss: Theory and experiments, Journal of Lightwave Technology **38**, 1668 (2020).

[67] The quantity $\mathrm{PDL_{dB}}$ is defined as the power ratio, in decibel, between the least and most attenuated polarization states, which yields $\mathrm{PDL_{dB}} = 20\log_{10}(e)\,\gamma$.